Robust Correction of Relative Geometric Errors Among GaoFen-7 Regional Stereo Images Based on Posteriori Compensation

Yingdong Pi, Bo Yang, Xin Li, and Mi Wang

***Abstract*—Correcting the relative geometric errors is an essential step in the generation of digital ortho maps and digital surface models from GaoFen-7 (GF-7) regional images, in which the block adjustment (BA) technology is always adopted. However, the traditional BA methods are typically ineffective and not universal due to their dependence on sufficient control data. Although recently developed BA methods using a large number of observation images can substantially eliminate the additional control data, they are not suitable for the BA with few images in the absence of sufficient control data, which is a situation that is often encountered in practical applications. In such situation, the inevitable elevation error caused by the initial positioning error of images will transfer and accumulate in the horizontal direction of the block, resulting in the inconsistent geometric accuracies among images. Aiming at this problem, this article proposed a practical method of combining a stable free BA and *a posteriori* compensation. Through the stepwise correction and integration of geometric errors, the elevation error and its cumulative effect in free BA could be eliminated at a small control cost, and a robust result with consistent accuracy could be achieved, even with only a few observation images. This method was validated through experiments performed on GF-7 stereo images, and the satisfactory results indicated that it effectively restrained error accumulation and improved the geo-positioning consistency of regional GF-7 images.**

***Index Terms*—Elevation error, free block adjustment (BA), GaoFen-7 (GF-7) regional images, posteriori compensation, relative geometric error.**

I. Introduction

GAOFEN-7 (GF-7) is China's first civil sub-meter high-resolution optical transmission stereo mapping satellite, and was successfully launched in November 2019. It operates on a sun synchronous return circular orbit at a height of 505 km, and its observation range is between the global northern and southern latitudes of 80 degrees. The satellite is mainly used for China's 1:10000 scale stereo mapping and the updating of higher-scale basic geographic information products. The stereo imaging system aboard the satellite is composed of two linear array push-broom optical cameras with forward (FWD) and backward (BWD) views. As shown in Fig. 1, the FWD and BWD cameras are arranged longitudinally along the flight direction of the satellite, in which the lines of sight of the FWD and BWD cameras are tilted 26° and −5° from the nadir view, forming a sufficient stereo intersection angle (IA) for observation. The main characteristics of the BWD and FWD cameras are given in Table I.

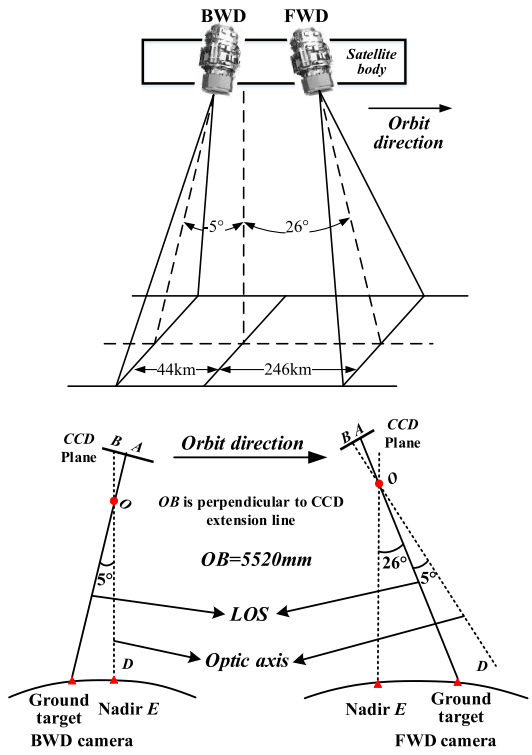

Fig. 1. Stereo cameras of GF-7satellite.

To register and fuse GF-7 images, and generate high-precision digital surface models (DSMs) and digital ortho maps (DOMs) from these images, the relative geometric errors in the imaging model must be fairly amended. Although the systematic geometric errors of images have been compensated for by on-orbit geometric calibration in the commissioning phase [1], [2], the remaining random attitude and orbit errors still cause significant

Manuscript received November 24, 2021; revised December 13, 2021, February 10, 2022, and March 15, 2022; accepted April 18, 2022. Date of publication April 26, 2022; date of current version May 4, 2022. This work was supported in part by the National Natural Science Foundation of China under Grant 42192583 and Grant 41601492 and in part by the Project funded by China Postdoctoral Science Foundation under Grant 2021TQ0247. *(Corresponding author: Bo Yang.)*

The authors are with the State Key Laboratory of Information Engineering in Surveying, Mapping and Remote Sensing, and School of Resource and Environmental Sciences, Wuhan University, Wuhan 430079, China (e-mail: pyd_imars@whu.edu.cn; 93341186@qq.com; xli2126@whu.edu.cn; wangmi@whu.edu.cn).

Digital Object Identifier 10.1109/JSTARS.2022.3169474

TABLE I
PARAMETERS OF THE CAMERAS ON THE GF-7 SATELLITE

Characteristics	BWD camera	FWD camera
Focal length (mm)	5520	5520
Pixel size (μm)	7.0	7.0
Swath (km)	20	20
Ground sample distance (m)	0.65	0.8
Field of view (°)	2.7	2.7

relative geometric errors among images. Therefore, as the key technology to correct the geometric error of regional remote sensing images, a block adjustment (BA) is essential to ensure the geometric accuracy of follow-up DOM and DSM products [3], [4]. The traditional BA of satellite images often depends on a certain number of well-distributed ground control points (GCPs) [5], [6]. However, more than 60% of the land on the Earth's surface is difficult to access, including forests, deserts, and polar regions, and it is usually difficult to obtain enough high-precision GCPs for a practical BA process. If the few obtainable GCPs with limited accuracy are introduced into a BA, it may result in an inconsistent geo-positioning accuracy among images due to the uneven constraints of the GCPs. Therefore, the possibility of a BA without GCPs has attracted much attention in the field of space photogrammetry [7]. In the absence of GCPs, two methods are generally used to achieve a high-precision BA. The first is to use alternative reference data to replace GCPs [8]–[12]. However, for GF-7 images with high geometric accuracy and spatial resolution, the available reference data are usually not easy to obtain. Another method is to construct a large-scale block with a large number of satellite images, and improve the BA accuracy by increasing the number of images [13]–[16]. The theoretical basis of this method is to treat the original geometric imaging models of images as observations with a certain degree of accuracy. According to sample statistics theory, the more observation samples, the higher the accuracy of the error estimation. Therefore, the BA accuracy can be improved by increasing the number of images [13]. However, the accuracy of this method depends entirely on the initial positioning accuracy of the images, the transmission and accumulation of elevation error in the block cannot be suppressed. Therefore, when the surveying area is small and there are few available images, the consistency of BA accuracy cannot be guaranteed.

In the absence of GCPs and other horizontal constraints, the BA accuracy depends on the initial positioning accuracies of the GF-7 images, which could be simply regarded as the weighted average of the initial accuracies [13], [14], [17]. Therefore, it is of little significance to discuss the absolute geo-positioning accuracy after geometric correction. The key point is how to achieve an image block with good relative geometric accuracy and uniform absolute geometric accuracy. If the relative geometric errors are well eliminated, the residual error of the whole block after geometric correction is mainly a horizontal translation, which can be easily corrected in the subsequent processing. However, in a free BA without absolute horizontal and vertical constraints, only the coplanar condition of the corresponding rays cannot determine the accurate elevation. Thus, the initial geo-positioning errors of the GF-7 images will result in an elevation error across the whole block. Such geometric relationship without constraints not only makes the images deviate from the accurate elevation surface, but also leads to the propagation and accumulation of elevation error in the horizontal direction of the block. As a result, it is difficult to absolutely eliminate the relative geometric errors among the regional images only using a free BA.

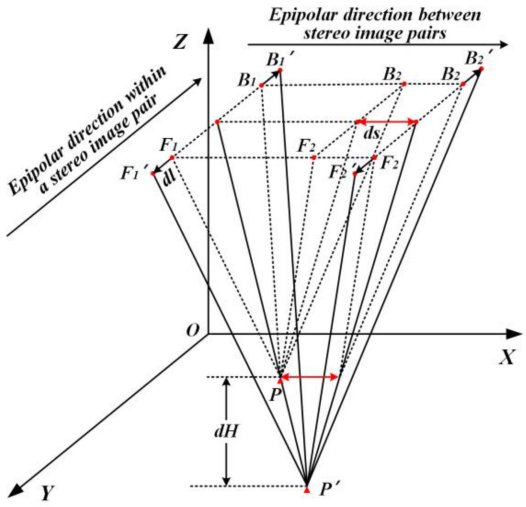

Fig. 2. Elevation error of GF-7 stereo images in a free BA.

To obtain a uniform geometric accuracy of regional images collected by the GF-7 satellite, a practical and robust relative geometric error correction method of combining a stable free BA and *a posteriori* compensation was proposed. First, we developed a stable free BA method to optimize the original random geometric error of images into a systematic geometric error. Second, the systematic elevation error of all regional stereo images was compensated for by available reference data. Finally, a free BA was performed again to solve the propagation and accumulation of positioning errors caused by elevation error. Generally, this method can eliminate the elevation error and its accumulation over the whole block, and achieve a consistent BA accuracy at a small control cost.

We built on previous studies in several ways. First, we analyzed the influence of elevation error in a free BA of GF-7 regional stereo images, established an error accumulation model, and clarified the propagation mechanism of elevation error. Second, we proposed a weighting strategy to overcome the weak intersection of tie points (TPs), to ensure the robust solution of a free BA, which lays the foundation for the stepwise processing mode. Third, we proposed a stepwise error correction method based on a posteriori compensation of elevation error, with the support of the systematicness of residual elevation error after the stable free BA, this method could achieve a satisfactory and consistent geometric accuracy using low cost control data.

II. ELEVATION ERROR AND ITS INFLUENCE IN THE FREE BA OF GF-7 IMAGES

As shown in Fig. 2, two stereo image pairs form an image block. Each image pair contains an FWD image and a BWD image, thus these two stereo image pairs can be referred to

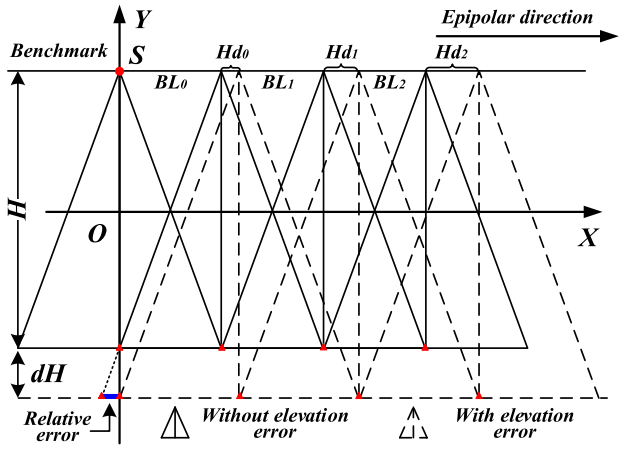

Fig. 3. Propagation and accumulation of elevation errors (taking the model on the left as the benchmark).

F_1B_1 and F_2B_2. In the ideal case (i.e., all images have no geopositioning error), the TPs on these two image pairs intersect at the object point P. But, due to the geopositioning error in the imaging models of F_1B_1 (*dl* in Fig. 2), the TP of this image pair actually intersect at the object point P'. However, even if there is a positioning error *dl* in the epipolar direction, the TPs also meet the coplanar constraint for this image pair. Thus, the geopositioning error in this direction cannot be eliminated. Further, in a free BA, to satisfy the coplanar constraint, the ideal geometric relationship between F_1B_1 and F_2B_2 is adjusted to ${F_1}'{B_1}'$ and ${F_2}'{B_2}'$. As a result, an elevation error dH and a cumulative geo-positioning error *ds* in the epipolar direction between the stereo image pairs will be generated, to ensure that TPs intersect at point P'. Fortunately, to meet the spatial intersection of all stereo pairs in the BA, this elevation error dH in the block is consistent theoretically, which is a result of the comprehensive effect of all images. Thus, the free BA of GF-7 stereo images will not only produce an inevitable elevation error, but also cause an accumulation of the horizontal geo-positioning errors across images. As shown in Fig. 3, when there is no elevation error, the corresponding rays intersect with each other, but when a systematic elevation error dH is introduced, the corresponding rays that should intersect on the ground will have relative errors in the epipolar direction. In a free BA, these errors will be eliminated based on the benchmark model, which will lead to the accumulation of errors along this direction (Hd_0, Hd_1, and Hd_2 in Fig. 3).

It was assumed that the elevation error was consistent after BA. From the above geometric relationship, the cumulative positioning error Hd_n caused by the elevation error dH on the *n*-scene image in the epipolar direction can be determined

$$Hd_n = \sum_{i=1}^{n} \left(\frac{BL_i \cdot dH}{H} \right) \tag{1}$$

in which, H is the height of the satellite orbit, BL_i is the length of the base line between the *i*th and $(i-1)$th images in the epipolar direction.

According to the above analysis and accumulation model, elevation error is a key factor that hinders a rigid BA result with consistent accuracy; thus its influence cannot be ignored. The influence of elevation error is closely related to the base–height ratio and IA. When the IA is small, its influence is limited, but its influence will become more significant with an increase in IA and the scale of the block.

III. Methodology

We developed a practical correction method based on a posteriori compensation, which uses a stepwise optimization strategy. As shown in Fig. 4, after the free BA process, the systematic elevation error in the BA was eliminated based on *a posteriori* compensation, and then the free BA was carried out again to further restrain the error accumulation caused by the elevation error. Finally, a rigid correction result with good relative geometric accuracy and uniform absolute geometric accuracy was obtained.

A. Stable Free BA Method

1) BA Model: The rational function model (RFM) is adopted as the basic imaging model of our BA method, which is widely used in the geometric process of satellite remote sensing imagery [18], [19]. Considering that the geometric imaging model of GF-7 images have been well calibrated, an affine transformation model is usually sufficient enough to correct the remaining geometric errors [13]–[20], therefore, the RFM, with an affine error correction model in imagery space, was adopted as the basic BA model here. The adopted affine model is shown in

$$\begin{cases} \Delta l = a_0 + a_1 s + a_2 l \\ \Delta s = b_0 + b_1 s + b_2 l \end{cases} \tag{2}$$

where $(\Delta l, \Delta s)$ is the correction for the image coordinates, (l, s) is the observations of the imagery coordinates, and $(a_0, a_1, a_2, b_0, b_1, b_2)$ is the affine model coefficients. Therefore, the basic BA model can then be established

$$\begin{cases} G_l = F_l(B, L, H) - l - \Delta l \\ G_s = F_s(B, L, H) - s - \Delta s \end{cases} \tag{3}$$

in which F_l and F_s are the ratio polynomials of RFM on the ground coordinates (B, L, H).

Additionally, because additional control data were not used, the BA was completely free in the horizontal direction and the coefficient matrix of the BA equation was rank deficient, leading to an unstable BA solution. To address this problem, virtual control points (VCPs) were introduced as weighted observations to reduce the spatial freedom of the entire block. Details of the generation and weighting of VCPs are provided in [13] and [20]. Therefore, the error equation for the VCPs and TPs could be derived by the linearization of the BA model (3)

$$\begin{cases} V_{vc} = A_{vc}x - L_{vc}\, P_{vc} \\ V_{tp} = A_{tp}x + B_{tp}t - L_{tp}P_{tp} \end{cases} \tag{4}$$

where V_{vc} and V_{tp} are the residual vectors of the VCP and TP, respectively; x is the correction vector for the BA parameters of all images; t is the correction vector of ground coordinates for the TPs; A_{vc} and A_{tp} are partial derivative matrices of BA parameters for the VCP and TP, respectively; B_{tp} is the partial derivative matrix on ground coordinates for TP; L_{vc} and L_{tp} are

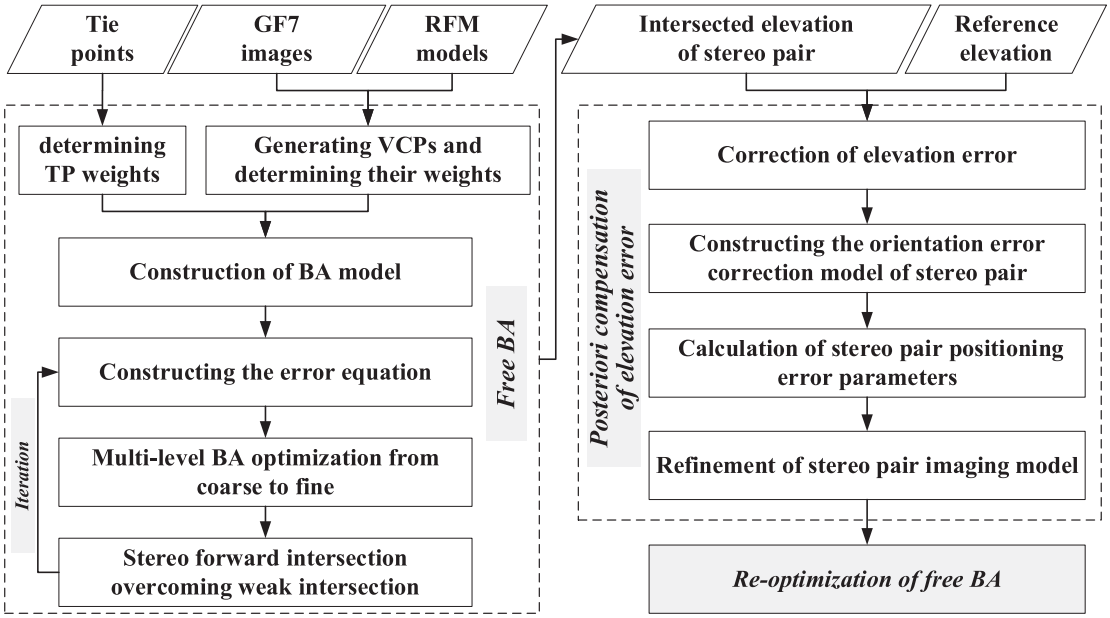

Fig. 4. Correction approach based on a posteriori compensation for GF-7 regional images.

the residual vectors calculated by the current BA parameters for the VCP and TP, respectively; and P_{vc} and P_{tp} are the weight matrices for the VCP and TP, respectively. In a BA system, the final error equation can be established by combining the error equations of all TPs and VCPs

$$V = Ax + Bt - LP \tag{5}$$

in which

$$V = \begin{bmatrix} V_{vc} \\ V_{tp} \end{bmatrix}, \quad A = \begin{bmatrix} A_{vc} \\ A_{tp} \end{bmatrix}, \quad B = \begin{bmatrix} 0 \\ B_{tp} \end{bmatrix}$$
$$L = \begin{bmatrix} L_{vc} \\ L_{tp} \end{bmatrix}, \quad P = \begin{bmatrix} P_{vc} & \\ & P_{tp} \end{bmatrix}.$$

2) Robust Free BA Solution: Due to the high orbit and narrow field of view characteristics of the GF-7 satellite, the IA among the large number of overlapping images in the BA is very small. For example, the IA between BWD overlapping images along the orbit is as small as 0°, while in the vertical orbit direction it is less than 2.3°. As a result, the intersection geometries of the TPs identified among these images by automatic matching is weak, which is almost inevitable in an automatic BA processing system. Such weak geometries will not only enlarge the elevation error of the TPs and affect the convergence accuracy of the elevation, but also result in the BA being unable to converge. In addition, due to the lack of constraints of the additional control constraints, the robustness of the BA system is weak, and the error correction model is prone to over parameterization, resulting in the propagation of errors and the deformation of the block [21].

To resolve these two problems, this article optimized the classical alternating approach BA solution method combining a least squares adjustment and the FWD intersection. The robust solution of our free BA was achieved by a BA optimization strategy from coarse to fine and the space forward intersection (SFI) overcoming the weak intersection geometry, respectively. The details are as follows.

a) Multilevel BA optimization from coarse to fine: There was a need to overcome the block deformation caused by the possible overparameterization of the error correction model in a free BA [21]. Referring to the idea of a spatial pyramid, we decomposed the solution of a high-order error correction model into the step-by-step solution from a low- to high-order model. The adopted affine model was decomposed into translation, similarity, and affine models from a low to high order. The estimation of the low-order model was used as the input of the least square solution of the high-order model, which avoided the allocation of low-order errors in the model to the higher order parameters and ensured the accuracy and reliability of the solution.

For the BA parameters at a certain order level, the normal equation can be deduced from the error (5) according to least square adjustment theory

$$\begin{bmatrix} A^TPA & A^TPB \\ B^TPA & B^TPB \end{bmatrix} \begin{bmatrix} x_k \\ t \end{bmatrix} = \begin{bmatrix} A^TPL \\ B^TPL \end{bmatrix} \tag{6}$$

in which, the unknown parameters to be solved include the correction of the BA parameters of all images x_k at this level and the correction of ground three-dimensional (3-D) coordinates of all TPs t. However, the number of TPs obtained by automatic matching is usually as high as tens of thousands or even hundreds of thousands, while the number of images to be adjusted is much less. It is difficult to solve these two kinds of unknowns together. Considering that the number of TPs is much larger than the number of images, the elimination method is often used in photogrammetry to eliminate the unknowns t, which will be updated by the subsequent SFI. Therefore, the estimation of x_k

can be deduced

$$\begin{cases} x_k = M^{-1}W \\ M = A^TPA - A^TPB(B^TPB)^{-1}B^TPA \\ W = A^TPL - A^TPB(B^TPB)^{-1}B^TPL \end{cases}. \quad (7)$$

The BA solution is a nested iterative process, in which the least squares adjustment at all levels is also an iterative process. When two successive adjustment solutions tend to be stable, the iterative solution ends. When all the iterative optimizations from the low- to high-order models ends, an overall iterative optimization is completed.

b) Stereo SFI overcoming weak intersection geometry: The base–height ratio (or IA) is the key index used to determine the accuracy of an SFI. Generally, when the IA is greater than 30° (the base–height ratio is greater than 0.55), the pair of TPs has a good intersection geometry and can intersect accurately on the ground. However, due to the complex spatial geometric relationship among the images in the block, there are a large number of weak intersection TPs even in the BA composed of stereo images. Directly deleting such TPs is extremely easy to cause uneven distribution of observations, and affect the consistency of the BA results. Therefore, it is necessary to include such observations in the BA solution. However, these TPs will not only reduce the accuracy and reliability of the SFI in the BA, but also prevent the BA solution from converging.

Given two arbitrary elevations H_1 and H_2, based on the initial RFM model of the images, the imagery relative geometric residual Δd between a TP on two images at these two elevations can be calculated. Then, the IA α can be estimated by $\alpha = \arctan(\Delta d/|H_2 - H_1|)$. For the TP on more than two images, we selected the largest angle among the images as its IA.

For the TPs with an IA greater than 30°, a satisfactory SFI can be achieved using the least square estimation of

$$\begin{cases} V_1 = D_1X - R_1 & P_1 \\ V_2 = D_2X - R_2 & P_2 \\ \vdots \quad \vdots & \vdots \quad \vdots \\ V_k = D_kX - R_k & P_k \end{cases} \quad (8)$$

where V_k is the residual vector *k*th point in a TP, D_k is the partial derivative matrix on the ground coordinate, which is deduced from the linearization of the RFM, R_k is the residual vector calculated by the current ground 3-D coordinate, P_k is the weight matrix, and $X = (dLon, dLat, dHei)$ is the correction of the ground 3-D coordinate of this TP.

For a TP with an IA less than 30°, we introduced an additional weighted constraint for elevation in the least square estimation to ensure the accuracy and reliability of the SFI

$$V_H = dHei \quad P_{Hei} \quad (9)$$

where $dHei$ is the correction of the intersected elevation in (8) and P_{Hei} is the weight of this introduced elevation constraint. This constraint can be considered to add an observation with a certain accuracy to the initial value of elevation, in which the key is to determine the weight P_{Hei}.

There is a relationship between weight and accuracy: $P_{Hei} = \sigma_0^2/\sigma_{Hei}^2$, where σ_0 is the accuracy of observations and σ_{Hei} is the elevation accuracy. Because the TPs are used as equal weight observations in the SFI, and can be ignored in determining P_{Hei}, the weight can be directly set as the reciprocal of the variance in the elevation accuracy. The elevation accuracy is closely related to the IA of a TP. When the IA is small, it is likely that the SFI solution will not converge. There should be a focus on the stability of the solution rather than the final intersected accuracy, because the influence of elevation error at a small IA is limited in the BA [22]. It is necessary to introduce a relatively strong elevation constraint for the TP with a small IA, that is, to give it a higher elevation accuracy. For the TP with a larger IA, the intersected elevation accuracy needs to be considered. Thus, a larger convergence space is used at the initial elevation value, that is, giving it a lower elevation accuracy, which is conducive to the adjustment of the convergence to the optimal state. Therefore, a linear elevation accuracy model with respect to the IA can be established

$$\sigma_{Hei} = (\sigma_2 - \sigma_1) \cdot \theta_{IA}/30 + \sigma_1 \quad (10)$$

where θ_{IA} is the IA of a TP, and its value range is [0, 30]; and $[\sigma_1, \sigma_2]$ is the preset elevation accuracy range, which is related to the initial accuracy of the elevation in the SFI solution. Generally, setting the range to [50, 300] can achieve a good BA result for GF-7 images.

B. A Posteriori Compensation of the Elevation Error

After the free BA, the initial random elevation errors are improved into a systematic error, which could be corrected at a small control cost with a posteriori compensation, instead of uniform distribution of control data required in an overall BA. All the reference data that can provide high-precision elevation, such as a DSM, laser altimetry data, or the GCPs, can be used to calculate the systematic elevation correction. First, the corresponding image points (CIPs) corresponding to these reference data are identified on the stereo image pair after BA (taking laser altimetry data as an example, the CIPs should be identified within its imagery spot range on the corresponding stereo image pair). Then, the intersected elevations from stereo image pair can be calculated using SFI. The offset of the intersected elevation relative to the elevation provided by the reference data is calculated. When the offset is calculated at multiple positions, the mean value is taken as the correction.

Then, we used the calculated correction to refine the positioning error of each stereo pair (correcting the relative positioning error of the stereo pair in the epipolar direction). As shown in Fig. 5, for each pair of GF-7 stereo images, taking the BWD image as the benchmark, the positioning deviation Δl of the FWD image in the epipolar direction (approximately along the orbit) was corrected according to the elevation error correction dH. Furthermore, the error correction model was obtained based on the RFM F_l in this direction

$$l + \Delta l = F_l(Lat, Lon, Hei + dH). \quad (11)$$

Finally, with the CIPs identified between the BWD and the FWD image as observations, the positioning model of the image was re-optimized using the estimated Δl. In addition, the imagery correction could be directly calculated according to the

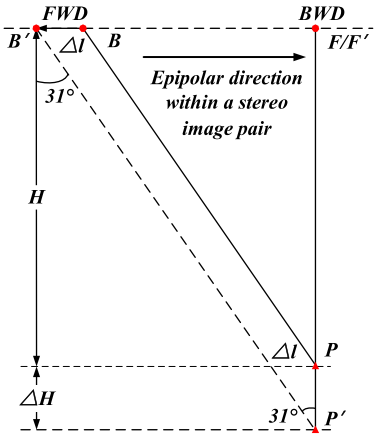

Fig. 5. Correction of the elevation error for two linear array stereo pairs.

TABLE II
DETAILS OF THE TEST AREA

Test area information	Parameter
Center position	43.5°N, 120.4°E
Area	About 8,777 km^2
Image number	12 pairs (24 scenes)
Maximum topographic relief	About 200 m

geometric relationship in Fig. 5 ($\Delta l \approx 0.6\, dH$), and the relevant parameters of the RFM were directly modified.

After the compensation of the elevation error, the free BA was performed again based on the compensated imaging models to further eliminate the accumulated positioning error caused by elevation error, and finally a reliable correction result with uniform geometric accuracy was obtained.

IV. EXPERIMENTS AND ANALYSIS

A. Dataset and Description of Experiments

We used a block composed of 12 stereo pairs (24 images) in Liaoning Province, China, for experimental verification. These images were collected by the GF-7 satellite between February and September 2020. All selected images were almost cloudless and had good radiation quality. The overlap between adjacent stereo image pairs across the orbit was larger than 50%, which was sufficient for the BA. Each image corresponded to an RPC file that recorded the imaging model. The geometries of these models were strictly calibrated in orbit, which compensated for the systematic geometric errors. The details of the test area are given in Table II.

The ATLAS laser point (LP) obtained from the ICESat-2 satellite was used for elevation error compensation and elevation accuracy verification. To ensure the reliability of the LP, we choose an LP with a slope less than 2° from the ATL08 product, which stores land elevation data [23]. The elevation accuracy of LPs in such a flat area was better than 0.5 m [24], which satisfied the accuracy requirements. Then, laser spots of 8.5-m radius were projected onto the images using the initial imaging models, and any significant CIPs measured within the spot range could be used as the imagery point of the LP, as shown in Fig. 6.

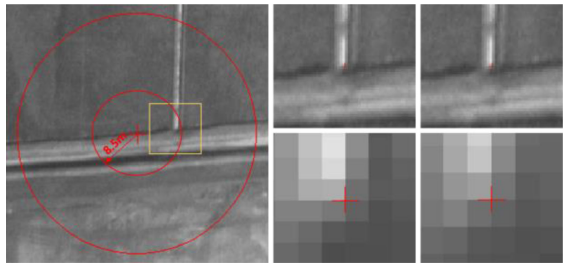

Fig. 6. Measurement of LPs on GF-7 stereo images (the right four images are enlarged images of the yellow box area on the original image, within which the CIP is identified).

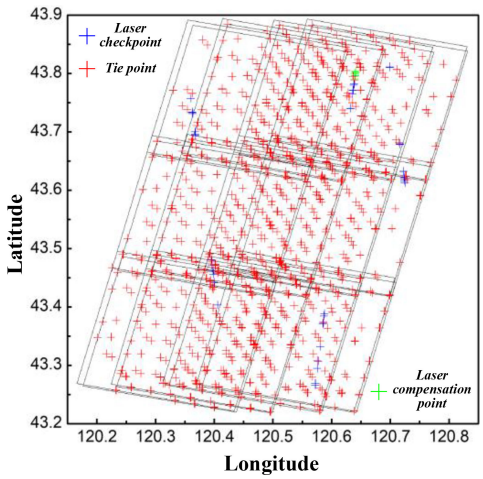

Fig. 7. Images and the observations in test area.

TABLE III
ELEVATION ACCURACY OF DIFFERENT PROCESSING STAGES (UNIT: M)

Processing stages	Checkpoint number	Mean	RMS	RMSE	Maximum
BFBA	44	4.04	6.87	5.55	15.85
AFBA	44	5.75	5.93	1.42	8.70
AFERC	34	0.29	1.46	1.43	2.90
ALBA	34	0.29	1.36	1.32	2.84

Using the high-precision matching algorithm based on SIFT [25], a total of 1528 pairs of reliable TPs were identified from the overlapping regions, and the maximum overlap of the TPs was six. Additionally, 44 ATLAS high-precision LPs were measured using the above method. The distribution of images, TPs, and LPs in the test area is shown in Fig. 7.

Based on the proposed approach, the relative geometric error correction was performed. First, a free BA was carried out based on the TPs and VCPs generated on each image. Then, the correction of elevation error was calculated using a cluster of LPs (ten green points) distributed in the upper right corner of the test area (to illustrate the advantage in using randomly and unevenly distributed elevation references). The estimated correction was 6.4 m, and the elevation error of all stereo pairs was compensated for by correcting the imaging model of each stereo image pair. Finally, the free BA was performed again based on the modified imaging models to further unify the geometric accuracies of regional images.

TABLE IV
RELATIVE GEOPOSITIONING ACCURACY OF STEREO PAIRS IN DIFFERENT PROCESSING STAGES

Stereo pair	CIP number	Processing stage	Longitude/m		Latitude/m		Elevation/m	
			Mean	RMS	Mean	RMS	Mean	RMS
P1–P2	210	BFBA	8.13	8.14	9.20	9.21	2.23	2.35
		AFBA	0.2	0.50	−0.08	0.41	−0.23	0.83
		ALBA	0.17	0.50	−0.08	0.41	−0.20	0.83
P2–P3	181	BFBA	1.83	1.84	−2.77	2.78	0.53	0.83
		AFBA	−0.11	0.24	−0.22	0.38	0.36	0.78
		ALBA	−0.10	0.23	−0.17	0.38	0.27	0.78
P3–P4	85	BFBA	0.95	1.00	0.36	0.48	−7.87	7.89
		AFBA	−0.06	0.29	0.12	0.37	0.47	0.83
		ALBA	−0.03	0.28	0.13	0.36	0.36	0.74

To illustrate the effectiveness of the proposed method in correcting the relative geometric errors, and restraining the cumulative effect of elevation error among the GF-7 regional images, the absolute elevation accuracy and the relative geopositioning accuracy of the images were verified through a series of experiments.

B. Verification of the Absolute Elevation Accuracy

The LPs were used as elevation checkpoints to verify the elevation accuracy of stereo image pairs. The 3-D ground coordinates corresponding to the CIPs of stereo image pairs were obtained by the SFI. Although the horizontal coordinates of the intersected ground points may be different from that of the LP, their elevations were consistent because they were measured within a flat spot. By calculating the difference between the two elevations, we obtained the elevation residual of each laser checkpoint, therefore the elevation accuracy could be verified. Table III gives the elevation accuracies in four processing stages (before the first free BA [BFBA], after the first free BA [AFBA], after the elevation error compensation [AFERC], and after the last free BA [ALBA]).

Before the BA, the RMS and the mean of the elevation residuals were 6.87 and 4.04 m, respectively, which indicated that there was not only an obvious elevation error but also a systematic offset in the elevation intersected by the initial stereo image pairs. Additionally, there was a certain difference between the RMS and the mean, and the RMSE was as high as 5.55 m, which further showed that the consistency of the elevations intersected by the stereo models was poor, and there were significant random positioning errors in the initial imaging models. At AFBA, the elevation error of the stereo image pairs was still significant, but the mean and the RMS tended to be the same. The RMSE was reduced to 1.4 m, which indicated that the elevation error of the different stereo image pairs was basically the same, and the elevation error of the whole block displayed a systematic offset. After further error compensation and the free BA, the mean of the elevation residuals was improved to better than 0.3 m, the RMS was improved to 1.36 m, and the maximum residual was less than three times the RMS; thus, the remaining systematic elevation error of the whole block was compensated for, and a local elevation anomaly was not generated over the whole block. As a result, the approach proposed here can effectively correct the elevation error, and restrain the accumulation of elevation error in a free BA.

C. Verification of the Relative Geopositioning Accuracy Between Stereo Image Pairs

Considering that the number of LPs in the test area was small and their distribution was not uniform enough to fully verify the correction performance, we further used the CIPs in the overlapping area of adjacent stereo image pairs to verify the relative geopositioning accuracy. Four stereo image pairs in the second row (three rows in total) of the block were selected to verify this accuracy. These four image pairs were recorded as $P1$, $P2$, $P3$, and $P4$ from left to right. First, a certain number of uniformly distributed reliable CIPs were identified in the overlapping area of two adjacent image pairs. The CIPs needed to have four degrees of overlap, that is, on the four images of two stereo pairs. Then, the ground coordinates corresponding to the CIP of each image pair were obtained through an SFI, and the difference between the ground coordinates of two stereo image pairs is the calculated relative geo-positioning residual. Finally, the relative geopositioning accuracy was obtained by counting the relative positioning residuals of all CIPs. Using the above method, the relative geo-positioning accuracy of three overlapping areas among the four stereo image pairs in three processing stages (BFBA, AFBA, and ALBA) of the BA was obtained, and the details are given in Table IV.

According to Table IV, in the BFBA stage there were obvious relative geo-positioning errors between the adjacent stereo image pairs in both the horizontal and elevation directions, and these errors were also inconsistent between different stereo pairs. The errors in both directions were well corrected in the AFBA stage. For these three pairs of overlapped stereo pairs, the comprehensive horizontal relative geo-positioning accuracies (longitude and latitude) were all better than 0.65 m, and the elevation accuracies were all better than 0.85 m according to the RMS. This result can meet the accuracy requirements of seamless splicing for subsequent terrain production, indicating the effectiveness of the proposed free BA method. After further elevation error compensation and a re-BA, the relative geopositioning accuracies did not change significantly and remained at a high level, which indicated that the method based on *a posteriori*

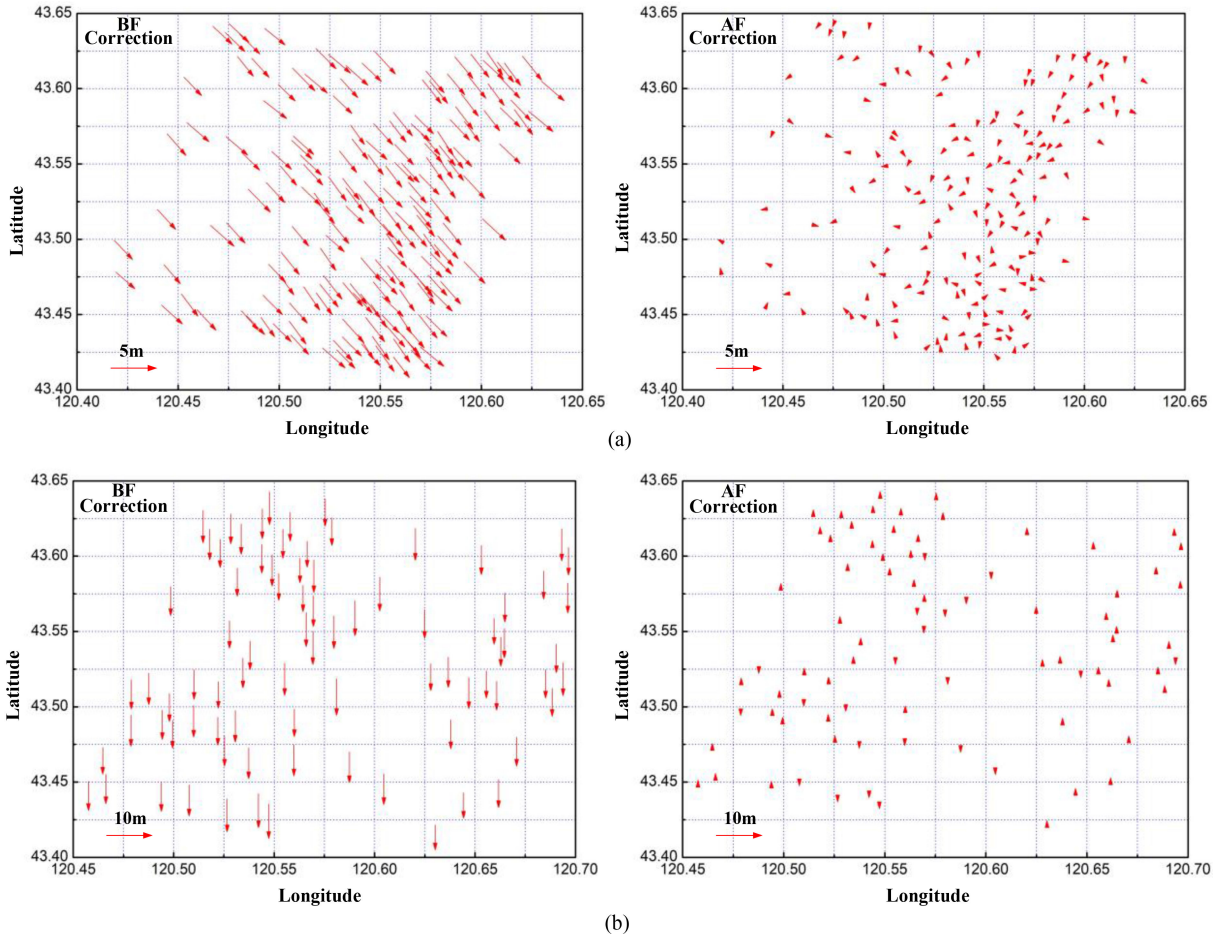

Fig. 8. Distribution of the ground relative geo-positioning residuals. (a) Distribution of the horizontal residuals between *P*2–*P*3. (b) Distribution of the elevation residuals between *P*3–*P*4.

compensation can correct the elevation error without damaging the relative geopositioning accuracy between stereo image pairs.

To illustrate the compensation performance on the relative geopositioning error between stereo pairs more clearly, the distribution of ground positioning residuals before and after correction was compared. Considering the distribution of the CIPs, the horizontal residuals between *P*2–*P*3 and the elevation residuals between *P*3–*P*4 are shown in Fig. 8. There was a significant relative geopositioning error between these two stereo image pairs before correction. Because the internal geometric accuracy within an image was consistent, the error had a systematic offset in the horizontal and elevation directions. After correction, this systematic error was well corrected, and the direction of the residual vectors displayed a strong randomness.

D. Verification of the Relative Geopositioning Accuracy Among Images

Based on the verification of the geopositioning accuracy between stereo image pairs, we further verified the relative geo-positioning accuracy of single images before and after error correction. The overall relative geo-positioning accuracy of all images in the whole block was verified using the TPs used in the free BA. First, the ground 3-D coordinates of each TP were obtained by the SFI, and then we projected this ground point to all corresponding images to obtain the imagery relative geopositioning residuals of this TP. Finally, the relative geopositioning accuracy of the whole block could be verified by counting all the imagery residuals of all TPs. We also verified the accuracies in three different correction stages (BFBA, AFBA, and ALBA), as given in Table V The relative geopositioning accuracy (RMS) of the whole block was improved from about 3.75 pixels before correction to about 0.5 pixels after correction, and the relative geometric error among the images were well eliminated, and

TABLE V
IMAGERY RELATIVE GEO-POSITIONING ACCURACY OF TPS

Processing stage	RMS/pixel			Maximum/pixel		
	Sample	Line	Sample_Line	Sample	Line	Sample_Line
BFBA	2.96	2.30	3.75	11.16	11.51	16.0
AFBA	0.42	0.37	0.56	2.38	1.83	3.0
ALBA	0.40	0.36	0.54	2.29	1.84	2.94

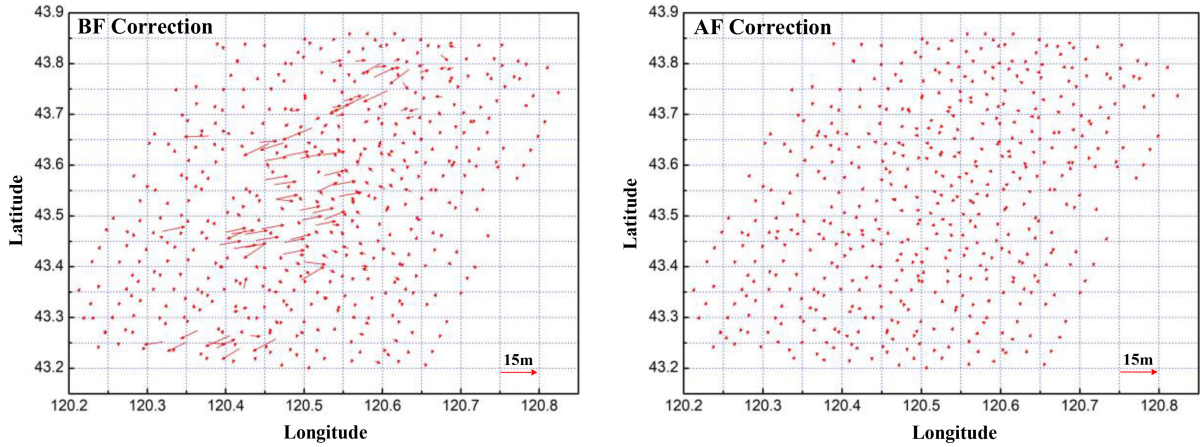

Fig. 9. Distribution of the relative geopositioning residuals of TPs over the whole block.

TABLE VI
RELATIVE GEOPOSITIONING ACCURACY BETWEEN ADJACENT BWD IMAGES

Image pair	Checkpoint number	BFBA/ pixel		AFBA/ pixel		ALBA/pixel	
		Sample	Line	Sample	Line	Sample	Line
P1–P2	69	0.45	–7.85	0.37	0.45	0.22	0.28
P2–P3	141	0.83	8.39	0.42	0.40	0.39	0.31
P3–P4	85	0.40	0.30	0.32	0.57	0.25	0.35

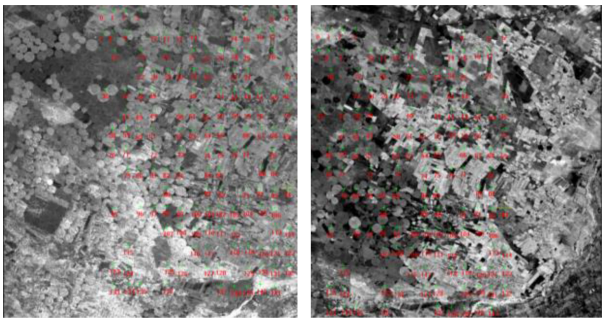

Fig. 10. Distribution of the checkpoints between *P*2–*P*3.

the geopositioning accuracy of the whole block tended to be consistent.

To express the optimization performance more clearly, 540 TPs were selected using the evenly distributed grids in the whole test area. Then, the vector distribution of relative geopositioning residuals of these TPs before and after correction was compared, as shown in Fig. 9. The size and direction of these residuals were disordered before correction, but after correction, all the residuals were close to zero, and their directions displayed a strong randomness. This indicated that the proposed method significantly improved the relative geo-positioning accuracy of the whole block.

The relative geopositioning accuracy between images was further verified using the checkpoints independent of the TPs. The above *P*1, *P*2, *P*3, and *P*4 image pairs were used to verify the accuracy of the BWD images and that of the FWD images relative to the BWD images. The CIPs identified on the overlapped regions of images were taken as checkpoints (see Fig. 10), and the relative geopositioning residuals of each pair of checkpoints were calculated with the support of a high-precision reference DSM.

Because the internal geometric accuracy of the images was relatively consistent, the relative geopositioning residuals of the checkpoints between two images was almost a systematic offset. Therefore, we only adopted the mean value of all the residuals as the accuracy index, as given in Tables VI and VII.

There were significant random relative geopositioning errors between images before error correction. At the AFBA stage, the initial random elevation errors in the block were improved to create a systematic elevation offset, but this offset accumulated in the horizontal direction of the block, resulting in an inconsistency of the geo-positioning accuracy of the images. Although there was no large relative geopositioning error between the BWD images with a small IA, a positioning error of up to 3.5 pixels was observed between the FWD and BWD images with a large IA. In addition, the positioning error caused by the elevation error accumulated linearly with the scale of the block, which could not be ignored in the relative geometric error correction of regional GF-7 images. After further elevation error compensation and a re-BA, the relative geopositioning accuracy between images was further improved. The relative geopositioning accuracies of these seven pairs of images in both directions were about 0.5 pixels, which fully met the accuracy requirements of seamless splicing.

The visual splicing of a pair of overlapping BWD images before and after correction is shown in Fig. 11. The relative geometric error between images was significantly improved by the proposed method, and the adjacent images met the requirements of seamless splicing.

TABLE VII
GEOPOSITIONING OF A FWD IMAGE RELATIVE TO A BWD IMAGE

Image pair	Checkpoint number	BFBA/ pixel		AFBA/ pixel		ALBA/pixel	
		Sample	Line	Sample	Line	Sample	Line
P1	89	0.20	−3.28	0.14	3.67	0.15	−0.53
P2	48	0.22	3.89	0.21	3.45	0.22	−0.67
P3	73	0.15	4.20	0.19	3.55	0.12	−0.60
P4	80	0.16	−1.92	0.12	3.87	0.15	−0.32

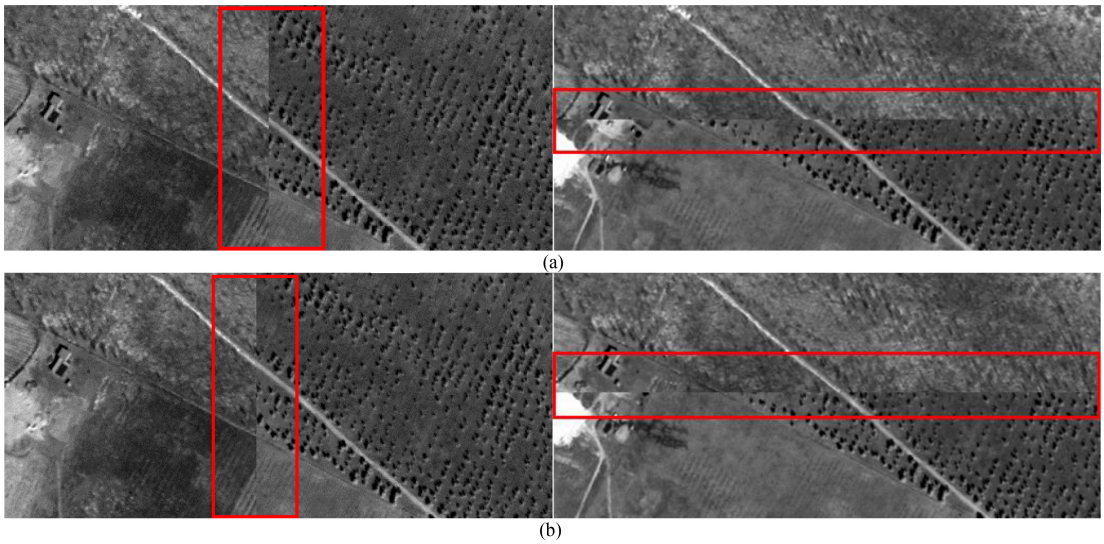

Fig. 11. Visual splicing effect of adjacent BWD images. (a) Visual splicing effect before the correction. (b) Visual splicing effect after the correction.

V. CONCLUSION

A practical relative geometric correction method was proposed for the high-precision geometric processing of regional GF-7 images. Based on a posteriori compensation of systematic elevation error resulted by a stable free BA, this method overcame the accumulation of elevation error at a small control cost, and obtained processing results with consistent accuracy and high reliability. The following conclusions were drawn from the article.

1) The experimental results indicated that this method improved the elevation and relative geometric errors among the GF-7 regional images effectively, which validated the effectiveness of our method.
2) The free BA based on multilevel BA optimization and the stereo SFI that overcame the weak intersection were feasible, which ensured the accuracy and reliability of the free BA, and optimized the random elevation errors to a systematic offset.
3) On the basis of the stable free BA, the *posteriori* compensation of the systematic elevation error not only corrected the elevation error, but also effectively restrained its accumulation, which was conducive to achieving a rigid BA result with consistent accuracy.

Overall, through the combined application of robust free BA and a posteriori compensation, the result of truly eliminating the relative geometric error among regional images is obtained at a small control cost, and there is no need for uniformly distributed elevation control, which makes this method more suitable for accurate geometric process in areas with unevenly distributed or inconsistent accuracy control data.

ACKNOWLEDGMENT

The authors would like to thank the anonymous reviewers for their constructive and suggestions and the China Center for Resources Satellite Data and Application for providing the experimental data. These supports are valuable.

REFERENCES

[1] D. Mulawa, "On-orbit geometric calibration of the orb-view3 high-resolution imaging satellite," *Int. Arch. Photogramm. Remote Sens. Spatial Inf. Sci.*, vol. 35, pp. 1–6, 2004.
[2] B. Yang, Y. Pi, X. Li, and Y. Yang, "Integrated geometric self-calibration of stereo cameras onboard the Ziyuan-3 satellite," *ISPRS J. Photogramm. Remote Sens.*, vol. 162, pp. 173–183, Feb. 2020.
[3] A. Bouillon, M. Bernard, P. Gigord, A. Orsoni, V. Rudowski, and A. Baudoin, "SPOT5 HRS geometric performances: Using block adjustment as a key issue to improve quality of DEM generation," *ISPRS J. Photogramm. Remote Sens.*, vol. 60, pp. 134–146, Apr. 2006.
[4] J. Poon, C. S. Fraser, and C. Zhang, "Digital surface models from high resolution satellite imagery," *Photogramm. Eng. Remote Sens.*, vol. 73, no. 11, pp. 1225–1232, Nov. 2007.
[5] L. Zhang, J. X. Zhang, X. Y. Chen, and H. An, "Block-Adjustment with SPOT-5Imagery and sparse GCPs based on RFM," *Acta Geodaetica et Cartographica Sinica*, vol. 38, no. 4, pp. 301–310, Aug. 2009.
[6] F. Rottensteiner, T. Weser, A. Lewis, and C. S. Fraser, "A strip adjustment approach for precise georeferencing of ALOS optical imagery," *IEEE Trans. Geosci. Remote Sens.*, vol. 47, no. 12, pp. 4083–4091, Dec. 2009.

[7] Q. Fu, S. Liu, X. Tong, and H. Wang, "Block adjustment of large-scale high resolution optical satellite imagery without GCPs based on the GPU," *ISPRS-Int. Arch. Photogramm. Remote Sens. Spatial Inf. Sci.*, vol. 42, pp. 91–94, Sep. 2019.
[8] T. Toutin, "Spatiotriangulation with multisensor VIR/SAR images," *IEEE Trans. Geosci. Remote Sens.*, vol. 42, no. 10, pp. 2096–2103, Oct. 2004.
[9] T. Toutin, "Spatiotriangulation with multisensor HR stereo-images," *IEEE Trans. Geosci. Remote Sens.*, vol. 44, no. 2, pp. 456–462, Feb. 2006.
[10] B. Wu, S. Tang, Q. Zhu, K. Y. Tong, H. Hu, and G. Li, "Geometric integration of high resolution satellite imagery and airborne LiDAR data for improved geo-positioning accuracy in metropolitan areas," *ISPRS J. Photogramm. Remote Sens.*, vol. 109, pp. 139–151, Nov. 2015.
[11] J. Lim and K. S. Lee, "Flood mapping using multisource remotely sensed data and logistic regression in the heterogeneous mountainous regions in North Korea," *Remote Sens.*, vol. 10, no. 7, pp. 1036–1052, Jul. 2018.
[12] J. Jeong, C. Yang, and T. Kim, "Geo-positioning accuracy using multiple-satellite images: IKONOS, quickbird, and KOMPSAT-2 stereo images," *Remote Sens*, vol. 7, no. 4, pp. 4449–4564, Apr. 2015.
[13] B. Yang, M. Wang, W. Xu, D. Li, J. Gong, and Y. Pi, "Large-scale block adjustment without use of ground control points based on the compensation of geometric calibration for ZY-3 images," *ISPRS J. Photogramm. Remote Sens.*, vol. 134, pp. 1–14, Dec. 2017.
[14] K. Liu, P. Tao, K. Tan, Y. Duan, J. He, and X. Luo, "Adaptive Re-weighted block adjustment for multi-coverage satellite stereo images without ground control points," *IEEE Access*, vol. 7, pp. 112120–112130, Aug. 2019.
[15] P. D. Angelo and P. Reinartz, "DSM based orientation of large stereo satellite image blocks," in *Proc. Int. Arch. Photogramm. Remote Sens. Spatial Inf. Sci.*, 2012, pp. 209–214.
[16] R. Passini, A. Blades, and K. Jacobsen, "Handling of large block of high resolution space images," *Int. Arch. Photogramm. Remote Sens*, vol. 36, pp. 1–6, 2005.
[17] Y. Zhang, M. Zheng, X. Xiong, and J. Xiong, "Multistrip bundle block adjustment of ZY-3 satellite imagery by rigorous sensor model without ground control point," *IEEE Geosci. Remote Sens. Lett.*, vol. 12, no. 4, pp. 865–869, Apr. 2015.
[18] C. S. Fraser, G. Dial, and J. Grodecki, "Sensor orientation via RPCs," *ISPRS J. Photogramm. Remote Sens.*, vol. 60, no. 3, pp. 182–194, May 2006.
[19] J. Grodecki and G. Dial, "Block adjustment of high-resolution satellite images described by rational polynomials," *Photogramm. Eng. Remote Sens*, vol. 69, no. 1, pp. 59–68, Jan. 2003.
[20] Y. Pi, B. Yang, X. Li, M. Wang, and Y. Cheng, "Large-scale planar block adjustment of Gaofen1 WFV images covering most of mainland China," *IEEE Trans. Geosci. Remote Sens.*, vol. 57, no. 3, pp. 1368–1379, Mar. 2019.
[21] D. R. Li, "On the signal-to-noise ratio in self-calibration block adjustment," *Acta Geodaetica et Cartographica Sinica*, vol. 11, no. 3, pp. 170–184, Aug. 1982.
[22] Y. D. Pi, B. Yang, and X. Li, "Block-adjustment and accuracy validation for GF4 Patch-images based on RFM," *Acta Geodaetica et Cartographica Sinica*, vol. 45, no. 12, pp. 1448–1454, Dec. 2016.
[23] A. Neuenschwander *et al.*, "Ice, cloud, and land elevation satellite 2 (ICESat-2) algorithm theoretical basis document (ATBD) for land-vegetation along-track products (ATL08) [OL]," 2020. [Online]. Available: https://nsidc.org/sites/nsidc.org/files/technical-references/ICESat2_ATL08_ATBD_r003
[24] M. Wang, Y. Wei, B. Yang, and X. Zhou, "Extraction and analysis of global elevation of control points from ICESat-2/ATLAS data," *Geomatics Inf. Sci. Wuhan Univ.*, vol. 46, no. 2, pp. 184–192, Feb. 2021.
[25] D. G. Lowe, "Distinctive image features from scale-invariant keypoints," *Int. J. Comput. Vis.*, vol. 60, no. 2, pp. 91–110, Jan. 2004.

Yingdong Pi received the B.Eng., M.Sc., and Ph.D. degrees in photogrammetry and remote sensing from Wuhan University, Wuhan, China, in 2014, 2017 and 2021, respectively.

He is currently a Postdoctoral Fellow with the State Key Laboratory of Information Engineering in Surveying, Mapping, and Remote Sensing of Wuhan University, Wuhan, China. His research interests include high precision remote sensing image processing and deep space detection.

Bo Yang received the B.Eng., M.Sc., and Ph.D. degrees in photogrammetry and remote sensing from Wuhan University, Wuhan, China, in 2005, 2009, and 2014, respectively.

Since 2014, he has been an Assistant Professor with the State Key Laboratory of Information Engineering in Surveying, Mapping, and Remote Sensing, Wuhan University, Wuhan, China. His research interests include automatic match, change detecting, and high precision geometric processing of remote sensing imagery.

Xin Li received the B.Eng., M.Sc., and Ph.D. degrees in photogrammetry and remote sensing from Wuhan University, Wuhan, China, in 1990, 1999, and 2006, respectively.

He is currently a Professor of the School of Remote Sensing and Information Engineering, Wuhan University. His research interests include the Photogrammetry and Remove Sensing, Industrial Measurement.

Mi Wang received the B.Eng., M.Sc., and Ph.D. degrees in photogrammetry and remote sensing from Wuhan University, Wuhan, China, in 1997, 1999, and 2001, respectively.

Since 2008, he has been a Professor with the State Key Laboratory of Information Engineering in Surveying, Mapping, and Remote Sensing, Wuhan University. His research interests include the measurable seamless stereo ortho-image databases, geographic information systems, and high precision remote sensing image processing.